Gold nanorod photoluminescence : applications to imaging and temperature sensing

Carattino, A.

A

SUPPLEMENTARY INFORMATION FOR: *In situ* TUNING OF GOLD NANOROD PLASMON THROUGH OXIDATIVE CYANIDE ETCHING

A

A.1. SOLUTION RESULTS

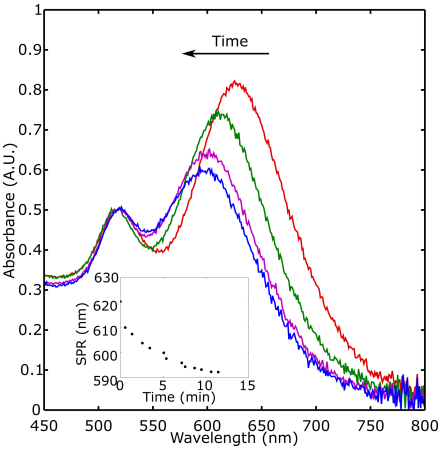

Figure A.1: Extinction spectra of a bulk suspension of gold nanorods dispersed in 100 μM KCN. The curves are displayed at 2 minutes intervals. The inset shows the peak position as a function of time. The curves were normalized to the transverse peak for clarity.

Figure SA.1 shows the behavior of nanorods dispersed in 100 μM KCN. The same sample than for the single-particle experiments was used. We observe a clear blue shift of the longitudinal plasmon resonance, towards the transverse peak at around 530 nm. As stated in the main text, we attribute the blue shift of the peak to a shortening of the long axis of the rods. This is because the CTAB is more efficient in protecting the sides than the tips of the particles. The blue shift does not seem stabilized for the last spectrum. We attribute this to a complete consumption of KCN by excess gold metal in our sample. If more KCN had been added, the blue-shift would probably have continued.

The spectra were acquired in an UV-Vis spectrometer. The first spectrum was acquired with the rods dispersed in water, before adding KCN into the cuvette. Later a solution such that the final concentration was 100 μM was added and a set of automatic spectra was recorded at a fixed interval of time. The peak position was extracted by fitting a double Lorentzian, one with a fixed central wavelength (the transverse resonance) and a second one for the longitudinal plasmon.

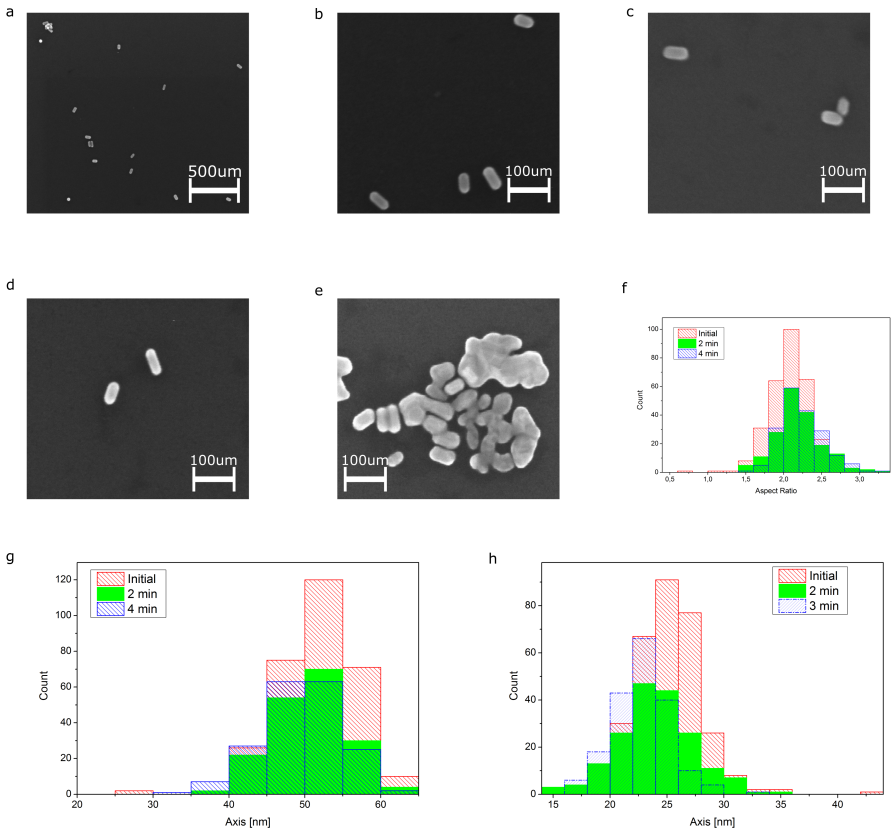

Figure A.2: SEM images of the rods a-b) after synthesis, at different magnifications c) after 2 minutes in 20 μM KCN. d) after 4 minutes in KCN and e) when they were forming clusters. f-h) Histograms of the aspect ratio (f), longitudinal(g) and transverse axis(h) before, after 2 and after 4 minutes in KCN. The distribution of values is too broad to visualize a shift in aspect ratio. Statistics on the values, however, show a slight increase and the data is summarized in table 1.

A.2. SEM IMAGES

Samples for SEM images were prepared by drop casting a suspension of gold nanorods into clean silicon wafers. An initial image of several hundreds of rods was acquired before any etching. The same samples were placed in a solution of KCN for 2 minutes and imaged again. Finally they were submersed again for 2 minutes in KCN and imaged afterwards. In this way, even if it was not possible to track the same particles during the etching process, it was possible to reproduce the conditions in which the reshaping took place on the optical microscope.

Figure SA.2 shows the SEM images of the rods. In SA.2a,b an example of the rods after synthesis and before etching at two different magnificatins. Figures SA.2c and d show the rods after 2 minutes and 4 minutes in 20 μM KCN. Figure SA.2e was acquired after 4 minutes in KCN; the difference on the shape of the particles when they are in contact is

notable. It has to be reminded however that the clusters of rods were already formed on the substrate before the etching started. Drop casting a suspension of rods tends to form conglomerates of particles rather than isolated particles as can be easily achieved by spin casting and shown in the optical experiments in the main text.

Histograms in Figures SA.2f-h show the analysis of the aspect ratio, the longitudinal and the transverse axes respectively for each of the cases. Table 1 summarizes the average values found after analyzing approximately 300 particles. The shift is rather small as compared to the standard deviation of the distribution of sizes.

	L (nm)	Sdv (nm)	D (nm)	Sdv (nm)
0min	51	5	24	3
2min	50	5	23	3
4min	49	5	22	2

Table A.1: Summary of the results obtained for 300 different particles while imaging them with an SEM. L and D are the length and diameter respectively. Sdv is the standard deviation of the values

A.3. BACKGROUND SPECTRUM

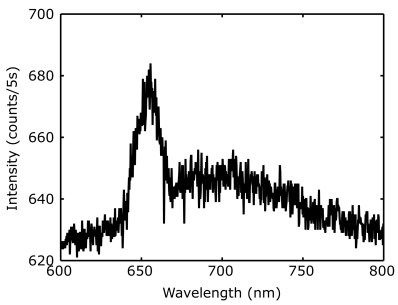

Figure A.3: Spectra from the background while exciting with a 532 nm laser. The peak appearing at 650 nm is attributed to Raman scattering from the O-H stretching modes of water.

Figure SA.3 shows the typical background when exciting with a 532 nm laser. The peak at 650 nm is attributed to Raman scattering from water. Normally this background can be well subtracted from the spectra acquired on particles. For less intense curves however, it is possible to observe a shoulder appearing at this particular wavelength. This indicates a non-additive phenomenon that we attributed to enhanced Raman scattering close to the nanoparticles.

B

Supplementary information for: Background Suppression in Imaging Gold Nanorods through Detection of Anti-Stokes Emission

B.1. SETUP

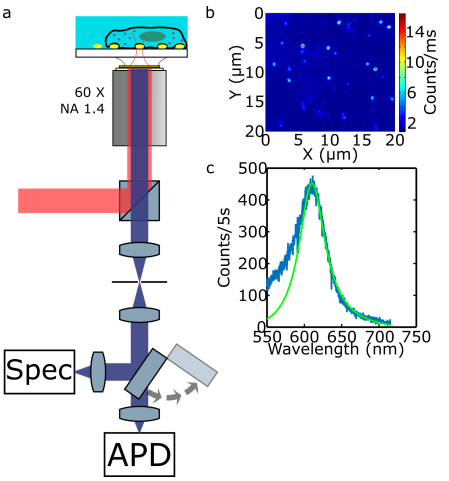

Figure B.1: Experimental setup and examples of observations. a) Simplified schematic of the confocal microscope employed during the measurements. b) A typical 1-photon luminescence raster scan of the sample immersed in water c) luminescence spectrum of a single rod.

Figure B.1 shows the schematic of the confocal microscope employed in the experiments. It is important to note the presence of a 50/50 beamsplitter before the objective. Exchanging it for an appropriate dichroic mirror would increase the collection efficiency. In this work we chose not to do it because the beamsplitter allows to collect both the full emission under 532 nm excitation and the Stokes/anti-Stokes emission under 633 nm without changes in the optical path.

B.2. UV-VIS SPECTRUM

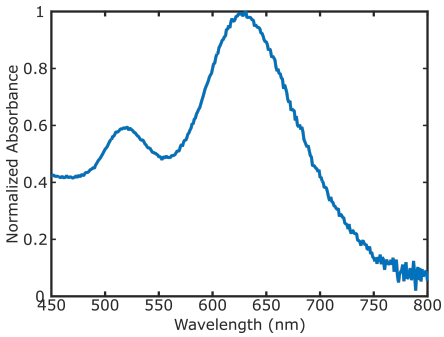

Figure B.2: Normalized extinction spectrum of a suspension of nanorods after synthesis. The resonance maximum is located at 630 nm.

Figure B.2 shows the extinction spectrum of the nanorod samples used throughout this work. Two peaks are clearly distinguishable, one around 630 nm that corresponds to the longitudinal plasmon resonance (LPR) of particles with sizes 50 nm × 23 nm and a second one at around 520 nm. This peak also includes contributions of spheres as by-products of the synthesis of the rods. The transverse plasmon resonance is also located at the same wavelength but is much weaker than the LPR. In a sample consisting exclusively of rods, the transverse resonance would be barely observable in a UV-Vis spectrometer.

B.3. FILTERS

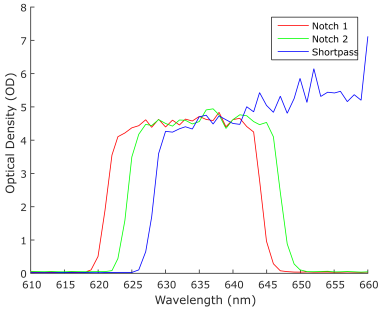

Figure B.3: Transmission spectrum of two notch filters and a short pass filter (Semrock).

The selection of filters plays a crucial role in the signal acquired. Since the main part of the anti-Stokes emission is concentrated around the excitation wavelength, it is important to select filters that have a high transmission close to the laser line. Figure B.3 shows the normalized absorption spectrum of two notch filters and a short pass. Both notch filters are branded as NF03 – 633E – 25 but show a slightly different absorption spectrum, shifted roughly 4 nm from each other. The shortpass filter (branded as SP01 – 633RU – 25) shows the transition to transmission even closer to the laser line.

For many fluorescence applications the exact shape of the transmission spectrum of the filters does not play a crucial role. However for anti-Stokes imaging, since the shape of the emission is exponential-like, minute changes in the transmission spectrum can have a great impact on the signal collected. For example, changing from a detection path with a spectrum like notch 1 to one like shortpass (i.e. shifting in about 7 nm the edge of the filter) increases the collected number of photons by about 50%.

In this work, since only one filter does not provide enough attenuation, care was taken to always employ the notch with the most favorable transmission spectrum in combination with either a shortpass or a longpass filter. Ideally, two shortpass filters would have been the best solution.

B.4. TEM IMAGES OF RODS

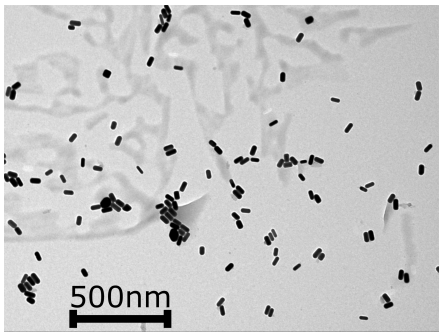

Figure B.4: TEM image of the nanorod sample. The scale bar is 500 μm.

Figure B.4 shows an example TEM image of the gold nanorod sample. Analysis on the dimensions of the particles yield an average length of 50 nm and diameter of 23 nm. This is consistent with the plasmon observed in fig. B.2 and at a single-particle level as in fig. B.1c.

B.5. WHITE LIGHT TRANSMISSION

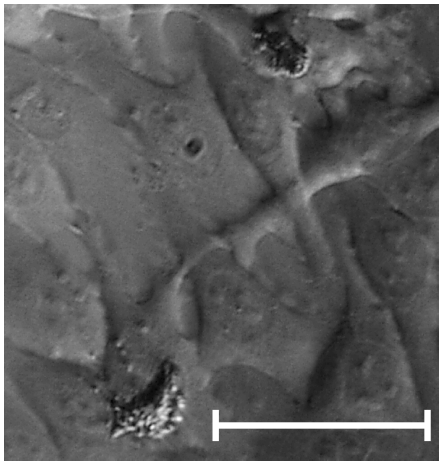

Figure B.5: White light transmission image of the sample with cells deposited on top of the rods. It is possible to observe that they cover entirely the observed region without spacing in between them. The scale bar in the figure is 20 μm in length.

B.6. FULL SCAN WITHOUT DYE

The raster scan shown in Figure B.6 corresponds to a larger area comprising the same region shown in the main text. The majority of the particles has a much larger contrast in

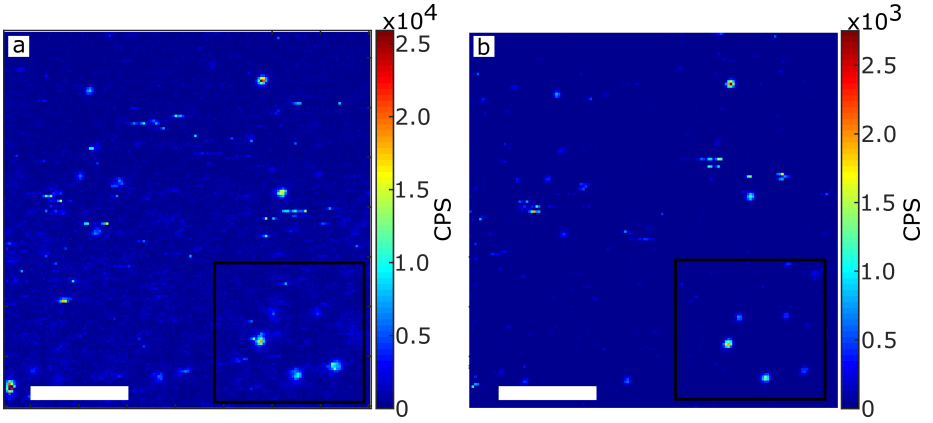

Figure B.6: Raster scan of a nanorod sample under HeLa cells using (a) a long pass filter and (b) a short pass filter for photoluminescence detection. Both scans contain the same region shown in the main text and here marked with a black square. The scale bar in both figures is 4 μm in length.

the anti-Stokes. Moreover it can be noted that the background is flat. In the Stokes image the nanorods are still visible, but the contrast is obviously lower.

B.7. FULL SCAN WITHOUT DYE

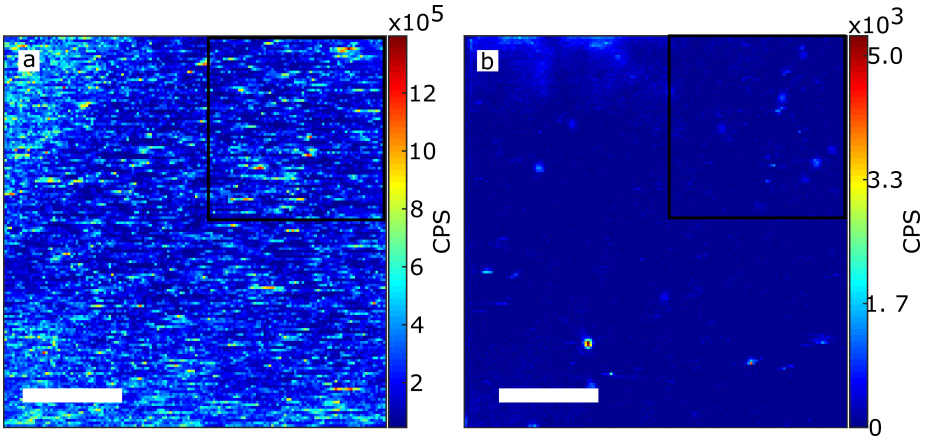

Figure B.7: Raster scan of a nanorod sample under stained HeLa cells using (a) a long pass filter and (b) a short pass filter for photoluminescence detection. Both scans contain the same region shown in the main text and here marked with a black square. The scale bar in both figures is 4 μm in length.

Figure B.7 shows a raster scan of gold nanorods under cells stained with ATTO 647N. Both images comprise the same region shown in the main text, here marked with a black square. No particles can be detected in the Stokes image, while several nanorods are visible in the anti-Stokes image with a high signal-to-background. We note, however, that

there is some background appearing in the top left part of the anti-Stokes image. This may be due to an increase of the concentration of ATTO 647N. The incubation procedure does not prevent the accumulation of dye in specific organelles of the cells, and there is no control on the final dye concentration.

B.8. SIGNAL-TO-BACKGROUND OF SEVERAL PARTICLES

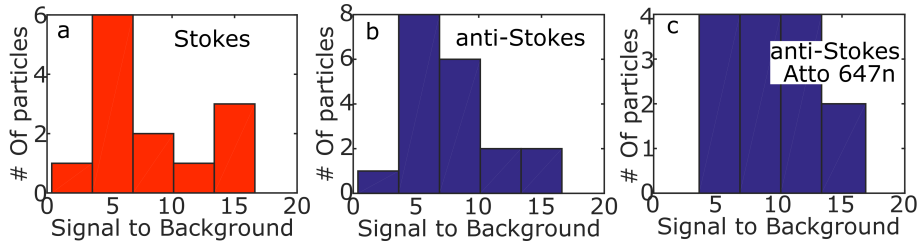

Figure B.8: Histograms of the signal-to-background of several particles irradiated at 30 kW/cm^2. a) Stokes emission under unstained cells, b) same but anti-Stokes emission, c) anti-Stokes under cells stained with ATTO 647N.

Figure B.8 shows the distribution of signal-to-background ratios for several particles. The data were acquired with an irradiation intensity of 30 kW/cm^2. Fig. B.8a shows the distribution for nanoparticles under unstained cells. It is possible to observe a broad distribution of values between ratios of 5 and 15. Fig. B.8b shows the signal-to-background distribution for the anti-Stokes emission, concentrated mainly between 5 and 10. Finally Figure B.8c shows the anti-Stokes signal-to-background ratio of particles under cells stained with ATTO 647N. In this case it is possible to observe a similar distribution of values. Stokes data under stained cells are not presented because it was impossible to detect single nanoparticles under those conditions.

B.9. VIABILITY TEST

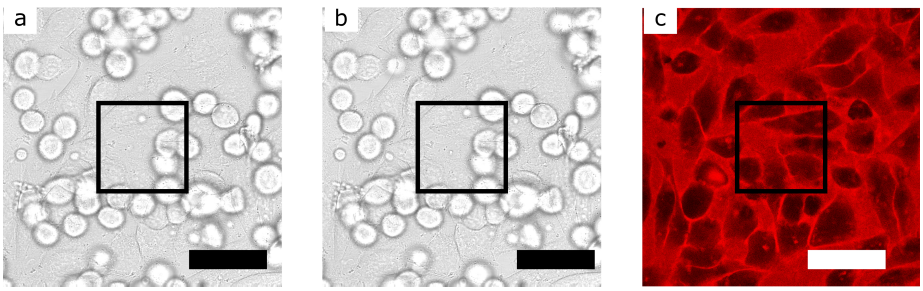

Figure B.9: White light transmission image of the cells, a) before being irradiated with the 633 nm laser, b) after the imaging process and c) viability test. The black square represents the imaged area. The scale bar is 50 μm.

To support the claim of the harmlessness of the method proposed in this work, we

performed a standard viability test of the cells after imaging. Figure B.9 shows white light transmission images of the cells. The left figure is before the imaging of the nanorods, the central is after and the rightmost is the result of a viability test with trypan blue. The black square represents the area that was imaged with the confocal microscope. The cells show no change between before and after the procedure. Moreover in Fig. B.9c it is possible to see that the dye did not enter the cells, therefore their membrane was intact after the imaging process.

More rigorous tests of viability after imaging the nanorods inside the cells are needed, but they are outside the scope of this work. On one hand there is enough evidence showing that gold nanoparticles are not toxic for cells[1, 2]. On the other hand two photon imaging[3] or photothermal heterodyne detection[4] of particles inside cells did not destroy them. Continuous wave confocal imaging as presented here however was not studied in detail in the past mainly because of the poor signal-to-background ratio with the normal Stokes configuration.

REFERENCES

[1] T. B. Huff, M. N. Hansen, Y. Zhao, J.-x. Cheng, and A. Wei, *Controlling the Cellular Uptake of Gold Nanorods,* Langmuir **23**, 1596 (2007).

[2] N. Lewinski, V. Colvin, and R. Drezek, *Cytotoxicity of nanopartides,* Small **4**, 26 (2008).

[3] B. van den Broek, B. Ashcroft, T. H. Oosterkamp, and J. van Noort, *Parallel Nanometric 3D Tracking of Intracellular Gold Nanorods Using Multifocal Two-Photon Microscopy,* Nano Lett. **13**, 980 (2013).

[4] C. Leduc, S. Si, J. Gautier, M. Soto-Ribeiro, B. Wehrle-Haller, A. Gautreau, G. Giannone, L. Cognet, and B. Lounis, *A highly specific gold nanoprobe for live-cell single-molecule imaging.* Nano Lett. **13**, 1489 (2013).

C

Supplementary information for: Gold nanorods as nano-thermometers

C.1. COMPARING COMSOL AND A SIMPLE APPROXIMATION FOR TEMPERATURE CALCULATION

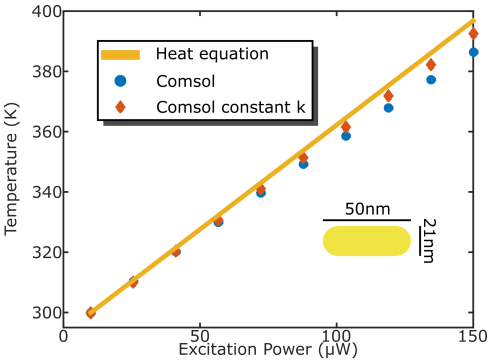

Figure C.1: Calculated temperature for a 21 nm × 50 nm nanorod under different excitation intensities. The full line is the result of the simple model while the dots are the calculated values using Comsol. The circles are with the default heat conductivity and the diamonds are with a constant value.

Throughout the main text the temperature measured with the anti-Stokes emission is compared to the calculated temperature using a simple heat diffusion equation. For spheres, assuming a thermal conductivity much higher than the surrounding medium, the temperature increase is given by

$$\Delta T(P) = \frac{P}{4\pi k_{\text{water}} R} \tag{C.1}$$

where P is the dissipated power, k_{water} is the heat conductivity of water and R is the radius of the particle. The dissipated power can be easily derived from the cross section of the particle at a given wavelength and the intensity of the focused laser beam. For nanorods we assumed an equivalent radius such that the total area is preserved.

Figure C.1 shows the difference between the results from the equation (full line) and a finite element method calculation using Comsol (dots) for a nanorod of length 50 nm and diameter 21 nm. The cross section and dissipated power were kept the same. The blue circles are the results given by using the built-in material properties of water, i.e. a thermal conductivity that depends on temperature. The diamonds are the results when the thermal conductivity is fixed to $0.61\,\text{W}(\text{m}\cdot\text{K})^{-1}$. The difference is accentuated at higher temperatures.

C.2. LUMINESCENCE POWER DEPENDENCE

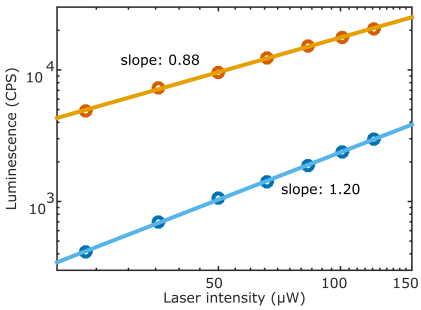

Figure C.2: Stokes and anti-Stokes emission as functions of excitation power. The linear fit in logarithmic scale has a slope of 0.88 and 1.20 respectively, confirming the 1-photon nature of both kinds of emission.

Figure C.2 shows the power dependence of both the Stokes and anti-Stokes luminescence. The fit in logarithmic scale confirms that both processes are due to one-photon absorption.

SUMMARY

Gold nanorods are ideal candidates for complementing fluorophores in labelling applications. The presence of the surface plasmon resonance generates large absorption and scattering cross sections, thus making the detection of single nanoparticles possible under a light microscope. The plasmon of gold nanorods depends on the ratio between their width and length and covers the range between 540 nm for spheres and even above 800 nm for elongated particles, thus almost the entire visible and near-infrared spectrum. The surface plasmon presents great opportunities in (bio-)sensing, enhanced spectroscopies, photothermal therapy and for concentrating light below the diffraction limit.

Chapter 1 of this thesis is a brief overview on fluorescence microscopy and on the basic properties of gold nanoparticles. Microscopy and specifically fluorescence microscopy is the result of a long process of technical improvements in optics and light sources, but also of the labels used to prepare the samples. From simpler molecules to genetically encoded proteins, the wealth of resources available nowadays is remarkable. In this context, gold nanoparticles can find their way because of their stability over time.

The resonance wavelength (or energy) of metallic nanoparticles will be given by their geometry and by the surrounding medium's properties, such as its refractive index. The geometry of the particles is determined during the synthesis procedure, where the average length and width can be tuned. Once the particles are deposited on a substrate, their resonance is already determined. It is possible, however, to induce shape modification to the particles through chemical means.

Previous works have focused on bulk measurements in suspension. In this case, the tips of the particles tend to be more reactive because they are less protected by the surfactants that prevent aggregation of particles. This leads to an anisotropic reaction that slowly transforms elongated particles into spheres and that softens sharp edges or tips, yielding an overall blue-shift of the resonance.

Chapter 2 shows that through well known chemistry between gold and cyanide ions it is possible to induce a red-shift of the plasmon. This is modelled through an isotropic etching of the particles, and a good agreement between calculations and experiments is obtained. The main difference with previous work is the absence of a capping agent on the particles' surface. Controllably changing the shape of nanoparticles is of great importance for experiments where a specific resonance is needed.

When particles are excited by a monochromatic light source, such as a laser, they will emit light at different wavelengths than the excitation wavelength. This emission is generally referred to as luminescence and is commonly used for imaging and tracking nanoparticles under confocal microscopes. When the excitation wavelength coincides with the plasmon resonance, the emission will happen not only at longer wavelengths, i.e. lower energies, but also at shorter wavelengths. This emission is called anti-Stokes emission and possesses intriguing properties.

Chapter 3 shows that it is possible to image gold nanorods in biologically relevant conditions through detection of their anti-Stokes emission. By placing a short-pass filter in the detection path the background level is reduced significantly, while the luminescence signal from the particles remains high. This is valid even for cells stained with a dye with high quantum yield that absorbs light of the same wavelengths as the rods. In these conditions it is not possible to observe any single nanoparticle through conventional Stokes-shifted emission while the anti-Stokes scheme presents a signal-to-background ratio higher than 10.

The technique presented in chapter 3 can be readily implemented in any conventional microscope by the addition of the appropriate filters. It does not require any special operation nor infrastructure. Moreover any data analysis tool for tracking, imaging, centroid extraction, etc. of single labels can readily be implemented without further modifications. The results of chapter 3 can have a major impact in the way nanoparticles are imaged and detected in biological conditions.

During the past two decades there has been an increasing interest in gold nanoparticles as possible agents for medical treatments. The strong interaction between particles and light makes them ideal candidates not only for labelling but also for releasing heat into very localized environments. This simple approach can be used, for instance, to induce death of cancer cells and is normally referred to as plasmonic photo thermal therapy.

Chapter 4 focuses on the characterization of the mechanisms that give rise to anti-Stokes luminescence. Discarding multi-photon processes, photons with higher energies than the excitation energy require interactions with thermal baths. In a nanoparticle electrons and holes can interact with phonons before recombining radiatively. The distribution of phonons in gold follows Bose-Einstein statistics, where the only free parameter is the temperature. We therefore propose in the chapter that anti-Stokes emission can be used for sensing temperature at the nanoscale.

By carefully fitting the luminescence spectra of single gold nanorods and nanospheres it is possible to extract the surface temperature of the particles. The method presented in chapter 4 does not depend on any ad-hoc calibration and can be performed in any confocal microscope with a coupled spectrometer. The chapter shows the increase in temperature with increasing laser powers and also shows the changes that the luminescence spectra undergo when increasing the medium temperature. The calibration-free procedure is a major improvement over previous techniques in the field of nano-thermometry.

Luminescence is not the only method for detecting gold nanorods with an optical microscope. Gold nanoparticles have a large scattering cross section coinciding with the plasmon resonance. Exciting nanoparticles with white light allows one to record the scattering spectra in any confocal microscope coupled to a spectrometer. Since the plasmon damping rate is affected by the surrounding conditions it can also be used to detect changes in temperature. From the mechanisms involved to explain the plasmon damping rate, only electron-phonon coupling is dependent on temperature.

Chapter 5 focuses on the characterization of the plasmon resonance of single gold nanorods at various temperatures. In the range of temperatures studied (between 293 K and 350 K), the plasmon width increases linearly with temperature. The broadening is assigned to an increase in the electron-phonon damping rate. Measuring the broadening

of the resonance can then be related to changes in temperature of the surrounding medium. The powers needed for recording scattering spectra are much lower than the ones employed when exciting the luminescence of the particles. However the broad distribution of widths and broadening rates found in the studies of chapter 5 does not allow to perform an absolute temperature measurement but only to measure a relative change.